www.czasopisma.pan.pl PAN POLSKA AKADEMIA NAUK www.journals.pan.pl

Oceanologia, 67 (4)/2025, 67408
Polish Academy of Sciences
Institute of Oceanology

https://doi.org/10.5697/DZVJ9279

Statistical downscaling of global climate projections over the Egyptian Red Sea coast

Mohamed Shaltout [1], Ahmed Abdelhamid [1], Ahmed Adel [1], Mohamed Gad [1, 2], Mohamed Elbessa [*, 1, 3]

Abstract

The long-term variability in atmospheric parameters plays a crucial role in shaping regional climate change. This study investigates the current and future characteristics of different surface atmospheric properties over the period 2011–2100 along the Egyptian Red Sea coast. First, the observed data were used to describe the short-term variability of weather conditions (2011–2021). Second, a bias correction statistical model based on the cumulative distribution functions (CDF) technique was developed by matching the four climate models [GFDL-ESM4; IPSL-CM6A-LR; MIROC6; MRI-ESM2-0] individually with daily observations over a 12-year overlapping period. Third, the resulting bias-correction models were applied to statistically downscale future projections of the studied atmospheric parameters under the Shared Socioeconomic Pathways (SSPs) scenarios. After bias correction, the outputs of each used climate model were averaged to calculate the ensemble mean for the period 2015–2100, improving accuracy and validity along ERSC at each of the five studied stations.

Our results indicate that, following bias correction the future scenarios of the Shared Socioeconomic Pathways (SSPs) show that the Egyptian Red Sea coast will experience significant changes with a wide range of uncertainty, with trends ranging from −0.14 to 2.91°C century^{-1}, −0.021 to 0.069 m s^{-1} century^{-1}, and −1.95 to 0.67 hPa century^{-1} for surface air temperature, wind speed, and sea level pressure, respectively.

Keywords

Red Sea; Statistical downscaling; Ensemble mean; SSPs; Climate conditions

[1] *Oceanography Department, Faculty of Science, Alexandria University, Alexandria, Egypt*
[2] *National Institute of Oceanography and Fisheries, NIOF, Cairo, Egypt*
[3] *College of Maritime Transport and Technology (CMTT), Arab Academy for Science, Technology and Maritime Transport (AASTMT), Abu-Qir, Alexandria, Egypt*
***Correspondence**: Mohamed.Abdelhameed_PG@alexu.edu.eg (M. Elbessa)

Received: 17 September 2024; **revised:** 17 September 2025; **accepted**: 25 September 2025

1. Introduction

Statistical downscaling has been successful in enhancing the quality and broadening the applicability of current and future atmospheric data by refining climate model outputs for specific stations. A challenging problem arises from the absence of actual observations of atmospheric data (e.g., surface air temperature, relative humidity, surface wind regime, and sea level pressure) along the Egyptian Red Sea coast (ERSC). Most studies on the ERSC have applied dynamic downscaling; accordingly, the current study can be considered the first attempt at applying statistical downscaling, which is often considered more accurate than dynamical downscaling for several reasons. First, statistical downscaling achieves higher resolution for local processes by utilising empirical relationships between large-scale climate variables (e.g., those derived from global climate models, GCMs) and local-scale conditions (Wilby and Wigley, 1997). Second, it is tailored to local observations, enhancing accuracy in representing regional variables such as temperature and precipitation (Maraun et al., 2010). Third, statistical methods are computationally efficient, allowing multiple simulations or ensemble analyses (Fowler et al., 2007). Fourth, they are flexible and can focus on specific phenomena, such as extreme events, which dynamic downscaling may not capture as effectively (Wilby and Wigley, 1997). Lastly, statistical downscaling inherently incorporates bias correction into GCM outputs, improving the reliability of future projections (Maraun et al., 2010).

In contrast, dynamical downscaling has limitations, including its reliance on GCM boundary conditions, which can introduce uncertainties (Wilby and Wigley, 1997). Additionally, it requires significant computational resources, limiting the number of scenarios that can feasibly be explored (Maraun et al., 2010). Even at high resolutions,

dynamical methods may not capture sub-grid-scale processes as effectively as statistical methods customised to specific regions (Fowler et al., 2007).

Therefore, statistical downscaling is crucial for reducing uncertainty in climate assessments within the study area, as it provides more detailed and localised climate information for both current conditions and future projections.

Long-term changes in temperature and weather patterns are referred to as climate change. In particular, Egypt is widely recognised as one of the nations most susceptible to the potential consequences arising from climate change. The Egyptian Red Sea coast (ERSC) is a hyper-arid zone (Middleton and Thomas 1992). Aridity zones are classified by the Aridity Index (AI = the ratio of average annual precipitation to potential evapotranspiration), which is less than 0.05 for a hyper-arid zone (UNESCO 1979; Middleton and Thomas 1992). A limited quantity of precipitation and minimal freshwater inflow from river runoff, in addition to the high rate of evaporation in this region, is among the highest globally, surpassing 2 m yr^{-1}. Consequently, it is widely acknowledged as one of Earth's most thermally elevated bodies of water. (Abualnaja et al., 2015; Gad et al., 2019).

The country's land and water resources face significant pressures due to high population density, rapid population growth, and widespread unregulated urbanisation. Egypt also struggles with limited technical capacity and community resilience in responding to extreme weather events. Global warming is anticipated to intensify Egypt's current water scarcity in its arid to semiarid climate, while contributing to increased heatwaves as well as more frequent and severe sand and dust storms. Climate change is expected to significantly impact various development sectors in Egypt, particularly water supplies, coastal and agricultural resources, tourism, and public health. Egypt's lack of institutional capacity to effectively monitor and regulate these pressures is likely to further exacerbate these impacts(Michel and Pandya, 2010).

The Red Sea exhibits a maximum width of 355 km in its southern half, while its minimum width is observed to be approximately 30–40 km at the Strait of Bab El-Mandab in the southern region. The Red Sea in Egypt reaches approximately 1200 kilometres, starting from Suez in the northern region (latitude 30°N) and reaching the Egypt/Sudan border in the southern region (latitude 22°N). The mean width of the Red Sea in Egypt is approximately 200 kilometres. At a latitude of 27°45'N, the Red Sea endures a division into two distinct bodies of water, forming a V-shape. To the west, it is referred to as the Gulf of Suez; to the east, it is known as the Gulf of Aqaba.

Its rich and diverse ecosystem distinguishes the Red Sea, making it a unique environment. The Egyptian Red Sea coastline is relatively narrow, shaped by a mountain chain running parallel to the shore. A significant presence of small gulfs and beaches further characterises the coast. Moreover, the study area contains numerous resources with strong potential to attract investment and stimulate diverse economic activities. Coral reefs and a mild climate would increase tourist attractions and mining resources. The Suez Canal, situated in the northern region, serves as a crucial link between the Red Sea and the Mediterranean, facilitating international maritime transportation and serving as a significant economic asset for Egypt. Together with major ports (Suez, Sharm El Sheikh, Nuweiba, and Safaga), it underscores the strategic and economic importance of the region. The population distribution is primarily concentrated in urban centres along the coast, with only scattered settlements in between. A significant concentration of renowned diving locations is found in the south, supported by abundant and diverse coral reefs and mangrove ecosystems. Most of the local population works in the resort cities that dominate the Red Sea coast. Undoubtedly, the tourism industry in the coastal area of Sinai and eastern Egypt, specifically along the Red Sea, constitutes a significant portion of Egypt's economic activities.

The Red Sea is characterised by four wind systems, each with different characteristics and origins (Langodan et al., 2017):

I. The north-to-south system is an extension of patterns observed in the Eastern Mediterranean Sea. This system exhibits a general tendency toward decreased intensity, which has been interpreted as a consequence of the observed reduction in storminess within the Mediterranean basin (Hochman et al., 2022).

II. The south-north system associated with the summer monsoon in the Arabian Sea forcing through the Bab-el-Mandeb Strait,

III. The Tokar Gap system is connected to the night cooling of the African plateau and the presence of the local Tokar Valley. This system is presented from June to September, with peak intensity typically occurring in July and August, depending also on the position of the Intertropical Convergence Zone (Turki et al.,2023). There is no definite significant trend in its intensity. The general wind systems along the axis of the Red Sea exhibit a more zonal nature, moving from west to east or east to west, and are associated with geographical gaps within the basin, such as the Tokar Gap. During the summer, there are eastward-blowing wind jets, primarily channelled through the Tokar Gap, while in the winter, there are westward-blowing wind jets originating from the Saudi Arabian margin, particularly over the northern Red Sea. These surface jets can reach wind speeds of 10–15 m s^{-1}; these wind patterns carried dust into the atmosphere over the Red Sea. Additionally, other

strong zonal winds, blowing from the Egyptian coast and moving eastward across the longitudinal axis of the Red Sea, can also contribute to the occurrence of dust storms (Jiang et al., 2009).

IV. Occasional winds blow from the narrow valleys on the upper Arabian side. These winds are not significant for the overall Red Sea regime.

Unfortunately, limited scientific studies related to climate projection have been performed on the ERSC; a significant knowledge gap exists compared to similar ecosystems (Acker, 2008). Thus, ERSC is an essential area in which further study of climate projection would be highly beneficial.

Numerous studies have identified variables such as air temperature, wind fields, relative humidity, and atmospheric pressure as key climate variables due to their substantial impact on various sectors of life (Bawadekji et al., 2022). Air temperature is a crucial parameter that significantly affects daily human activities; even slight changes can have noticeable effects. One of the leading climate challenges is the increase in relative humidity, which is calculated using surface air and dew point temperatures. However, rising surface air temperature is often associated with a decrease in relative humidity. The interaction between these factors can have severe consequences, particularly during heat waves, which may lead to higher rates of heat-related illnesses or fatalities (Sherwood and Huber, 2010).

An arid climate dominates the Red Sea Region, which is widely regarded as an extension of the vast Sahara Desert. The Mountain ranges along the Red Sea region give rise to a distinctive topographical feature that functions as a natural wind channel. This channel supports long-axis winds notable for their cloudy skies and drizzle, particularly during winter. The presence of the Red Sea trough influences the weather and climatic conditions, resulting in a range of annual rainfall ranging from 10 to 600 mm (Viswanadhapalli et al., 2017). Most of the region is situated within the subtropical high-pressure belt, characterised by significant Hadley cell subsidence.

For this study, we investigated surface air temperature, relative humidity, surface wind regime, and sea level pressure using statistical downscaling. Further details on previous studies addressing these parameters are provided in the literature.

1.1 Surface air temperature (T_{2m})

The Red Sea experiences a latitudinal gradient of increasing daily maximum temperature (Tmax) from north to south, driven by variations in solar energy. The thermal regimes of the Gulf of Suez and the Gulf of Aqaba are comparatively more relaxed than the southern region, which exhibits the highest thermal intensity. The timing of Tmax exhibits a discontinuous pattern within the Red Sea basin, characterised by a distinct transition occurring between the latitudes of 20°N and 22°N. The northern region of the Red Sea is experiencing a more noticeable warming trend than the southern region (Chaidez et al., 2017). The air temperature in the northern Red Sea exhibits its lowest value throughout the year, with recorded temperatures ranging from 6°C to 39°C at the Suez Canal and 13.5–42°C at Jeddah. There is a noticeable and rapid rise in temperature as one moves towards the southern latitudes below 26°N. The region with the highest temperatures in the Red Sea is between the latitudes of 20°N and 16°N. The average daily maximum temperature in January varies, ranging from approximately 20°C in the northernmost regions to around 29°C in the southernmost regions. In contrast, during July, these values increase to approximately 35°C in the north and 40°C in the south (Fouda and Gerges, 1994).

Edwards (1987) reported a significant variation in surface air temperature over the Red Sea basin, ranging from 15.5–30.0°C in Hurghada, 23.5–32.0°C in Jeddah, and 25.0–35.0°C in Massawa. In more detail, the southern region of the Red Sea basin has a higher surface air temperature than the northern Region (Al-Barakati and James 2002; Al-Subhi and Al-Aqsum 2008; Mohammed et al., 2010; Bruckner et al., 2012). Solar radiation reflected from mountains along the Red Sea Coast, especially in the city of Safaga, causes air temperature rises, which may explain why temperature increases southerly (El Saman and Mahmoud, 2016).

In the Red Sea region, the maximum temperature typically occurs for a short period in the afternoon, while the minimum is observed around sunrise. During the period 2012–2022, the minimum temperatures at Suez, Sharm El Sheikh, Safaga, and Marsa Alam were 1.2, 2.0, 0.3, and 5.3°C respectively, and the maximum temperature 41.8, 46.0, 36.4, and 45°C respectively, and the mean of 22.8, 26.9, 26.1, and 25.9°C respectively (Ayman et al., 2023).

During the period (2008–2020), the annual surface air temperature Min, Max, and mean at Suez were 23.5, 25.1, and 24.2°C, respectively. While at Safaga, the temperatures were 25.4, 27.0, and 26.1°C, respectively (Dawod et al., 2022).

1.2 Relative humidity (RH)

Since most of the air that enters the basin of the Red Sea is characterised by relatively low moisture content, the average annual humidity over the open Sea is maintained at approximately 70%. In the southern Red Sea, humidity levels show a marked seasonal contrast: higher in winter with prevailing southeasterly winds, and lower in summer with prevailing northwesterly winds. Along the coast, humidity is generally lower over the sea but shows an increasing trend from north to south (Fouda and Gerges, 1994). The distribution of relative humidity (RH) exhibits higher values during the summer months in the southwestern region of the research area, particularly near the Red Sea. The arid

climatic conditions in desert regions are associated with reduced RH levels observed in the eastern and western areas adjacent to the Red Sea.

Relative humidity in the air exceeds due to the mangrove swamps in Sharm El Bahri, which recorded the highest RH values along the Red Sea region (Kaunang and Medellu, 2013). Fouda and Gerges (1994) reported that the relative humidity in the Red Sea region increases progressively from north to south. The relative humidity ranged between 31.7% at Safaga and 67.0% at Sharm El Bahri (El Saman and Mahmoud, 2016).

Relative humidity has a significant seasonal variability: it is driest in summer mornings and most humid during winter nights. The warm water of the Red Sea leads to an exceptionally high rate of evaporation, resulting in relative humidity levels often exceeding average values, where the average annual relative humidity over the open sea is typically around 70% with an interannual variability of $\pm$ 5%. During the period 2012–2022, the minimum RH at Suez, Sharm El Sheikh, Safaga, and Marsa Alam was 6.3, 3.9, 2.6, and 3.2% respectively, and the maximum was 99.2, 100, 98.6, and 100% respectively, and the mean of 51.6, 40.8, 42.9, and 41.2% respectively (Ayman et al., 2023).

1.3 Surface wind regime (WS_{10}, WD_{10})

During summer, southwesterly winds associated with the Indian summer monsoon traverse the African coast and enter the Red Sea through the Tokar Gap. These winds converge with the northwesterlies from the northern Red Sea as they progress toward the Gulf of Aden. The cross-equatorial flow facilitates moisture transport and plays a crucial role in regulating air temperature, bringing cool, humid air from the equatorial Arabian Sea into the western Red Sea. In winter, the northwest and southeast wind systems transport moisture from both the northern and southern regions surrounding the Red Sea. When these contrasting systems converge above the Red Sea, the moisture is transported through the Tokar gap towards the western direction and, on occasion, towards the eastern direction, contingent upon favourable circumstances. Winter temperatures are lower than summer temperatures due to the influx of cool and humid air from the Northern Region of the Red Sea. The summer monsoon current originating from India, which passes through the African subcontinent, plays a significant role in shaping temperatures during the summer season.

In contrast to other regions within the Red Sea area, introducing moisture to this area during the summer monsoon originating from the Arabian Sea decreases the temperatures experienced during the summer. The spatial distribution and magnitude of the Rossby Subtropical Counter Current (RSCZ) are contingent upon the relative intensity of the prevailing northwesterly and southeasterly wind patterns. The frequency of heavy rainfall over the central Red Sea region is determined by the quantity of moisture lifted orographically over the coast and the nearby mountain areas. The southern Red Sea and its adjacent areas primarily depend on a narrow southeastern wind branch to obtain moisture during the winter. In contrast, the northwest wind branch produces cold air that is also moist. The primary factors contributing to precipitation within the RSCZ are the presence of moisture and temperature differentials. Convective rainfall occurs in the northeastern region during the winter season. It is characterised by the convergence of warm, arid air masses originating from one direction with cold, moist air masses originating from another. The upward frontal lifting leads to convection and episodes of heightened precipitation. Convective precipitation is observed to occur in conjunction with significant temperature differentials resulting from the transfer of moisture between warm and cold air masses traversing the Red Sea region (Viswanadhapalli et al., 2017).

The wind patterns along the ERSC are primarily shaped by local wind systems, resulting in a prevailing northwestern to northeastern direction throughout most of the year. Documented wind patterns, such as anabatic, katabatic, and sea-land breezes, lead to elevated wind velocities within specific time intervals (09:00–16:00) daily (Tonbol et al., 2019).Orographic factors primarily affect the wind patterns in the Red Sea due to the heightened mountain ranges along its eastern and western coastlines (Sofianos and Johns, 2007). The average wind speed indicates a general increase toward the north. The presence of coastal mountain ranges significantly influences the direction and speed of surface winds, causing them to align with the axis of the Red Sea basin (Patzert, 1974). The prevailing winds in the Red Sea are primarily from the northwest, with typical velocities ranging between 4 m s^{-1} and 9 m s^{-1} (Menezes et al., 2018). The wind system in this region is additionally impacted by weather patterns originating in the eastern Mediterranean (Pedgley, 1974). During the winter months, a wind stream blowing westward can be observed along the northwestern coast of Saudi Arabia. This wind stream has the potential to induce substantial evaporation and heat loss along the northeastern coast of the Red Sea, and it may also facilitate deep-water convection (Eladawy et al., 2017). The geological processes responsible for the formation of the Red Sea have also resulted in elevated mountain ranges surrounding the basin. The presence of these ranges significantly influences the prevailing wind patterns in the region, effectively transforming the Red Sea into a wind corridor characterised by the dominance of winds that align with its axis. Most mountains reach elevations greater than 1500 m. The mountains along the Red Sea axis are crucial in redirecting the northeast monsoon winds from the Arabian Sea toward the southeast. During the summer, the prevailing wind pattern in the basin is characterised by northwesterly winds.

Conversely, the Red Sea Convergence Zone forms in winter due to the convergence between the orographi-

cally induced southeasterly winds in the middle Red Sea and the northwesterly windstorm from the Mediterranean Sea (Langodan et al., 2017). The dominant wind direction and precipitation patterns are typically influenced by the northeast monsoon during winter and the southwest monsoon during summer. The dominant wind pattern in the northern Red Sea is characterised by a consistent north-northwesterly direction throughout the year, with occasional southerly winds occurring during the winter season. In regions located south of the 20°N latitude, the dominant wind direction during the summer months is northerly, whereas during the winter season, it tends to originate in the south-southeast. A state of intermediate conditions is observed in the Central Red Sea, characterised by northerly and southerly influences.

The region is distinguished by areas with relatively low atmospheric pressure, resulting in calm weather conditions. During the onset of summer, the intermediate zone undergoes a gradual southward movement, resulting in the seasonal shift in wind direction within the southern region of the Red Sea. Furthermore, within the coastal zone, a diurnal alteration of wind direction occurs, transitioning from offshore during daytime to onshore during nighttime. This phenomenon is primarily influenced by the contrasting heating and cooling patterns between the land and the sea. The Gulf of Aden experiences a reduction in the impact of the southwest monsoon due to the elevated mountains in its vicinity. Consequently, this region's prevailing wind direction is northwesterly during the summer. Throughout the remainder of the year, the northeast monsoon engenders easterly winds over the Gulf region, shifting to the southeast, specifically in the vicinity of Bab el Mandab (Fouda and Gerges, 1994).

The dominant wind direction over the Egyptian Red Sea Coast (ERSC) throughout the year predominantly varies from northwesterly to northeasterly. Winds from the southeasterly to southerly occur only briefly, accounting for about 5–10% of the time. This prevailing wind pattern is likely influenced by the elongated mountain ranges along the coastline. Additionally, a decreasing wind speed trend of $--0.15$ m s^{-1} annually has been observed at Safaga Harbour (Tonbol et al., 2019). Ayman et al. (2023) revealed that 65–70% of the wind directions over the ERSC are north, northwest, and west, while 10–15% of the time winds blow from the northeasterly direction, and the rest from other directions. During the period 2012–2022, the minimum wind speed at Suez, Sharm El Sheikh, Safaga, and Marsa Alam was 0 m s^{-1}; the maximum was 11.3, 6.9, 13.4, and 19.9 m s^{-1}, respectively, and the mean was 3.8, 4.4, 5.2, and 4.1 m s^{-1}, respectively.

1.4 Seal level pressure (SLP)

The annual variations of SLP during 2008–2020, as revealed by (Dawod et al., 2022), were 1012.8 hPa Min and 1014.7 hPa Max, with a mean of 1013.8 hPa at Suez; and 1010.5 hPa Min, 1012.3 hPa Max, with a mean of 1011.4 hPa at Safaga. In the same context, during the period 2012–2022, the minimum SLP at Suez, Sharm El Sheikh, Safaga, and Marsa Alam was 997.5, 996, 998.2, and 999 hPa, the maximum was 1032, 1029, 1028.6, and 1031 hPa respectively, and the mean was 1013.8, 1010.6, 1012.3, and 1011.6 hPa respectively (Ayman et al., 2023).

The atmospheric pressure monthly average in 2020 at Suez ranged from 1005.4 hPa in January to 1020.9 hPa in August, with an average of 1012.9 hPa. At Safaga, it ranged between 1003.3 hPa in July and 1020 hPa in January, with a mean of 1011.3 hPa. Otherwise, the annual variations of atmospheric pressure over 2008–2020 at Suez and Safaga revealed a common trend of decreasing pressure at Suez and increasing pressure at Safaga, where the atmospheric pressure average during this period at Suez ranges from 1012.8 hPa to 1014.7 hPa with an average of 1013.8 hPa. At Safaga, it ranged between 1010.5 hPa and 1012.3 hPa, with a mean of 1011.4 hPa (Dawod et al., 2022).

Despite numerous prior investigations aimed at examining the present state of atmospheric parameters along the ERSC, a recurring issue in previous analyses appears to be the limited duration of these studies. Therefore, conducting more extensive and long-term investigations is imperative to better understand the recent alterations in atmospheric parameters. However, it is worth noting that regional climatic modelling studies are scarce in the ERSC. Most of these studies rely on regional climatic models. Using statistical downscaling in the analysis will reinforce the findings of earlier modelling work and future improvements by addressing uncertainties. One potential method for addressing this issue is employing a recently developed technique, examining 43 years of contemporary atmospheric attributes, coupled with the statistical extra-

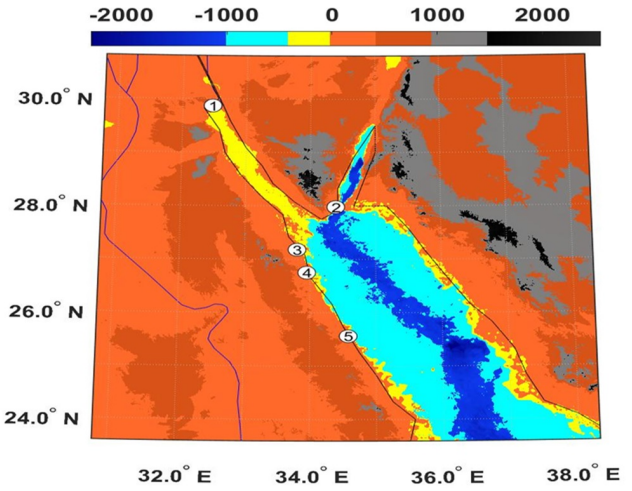

Figure 1. Topographic and bathymetric map of the study area with the five considered weather observation stations: 1) Suez, 2) Sharm El Sheikh, 3) Hurghada, 4) Safaga, and 5) Marsa Alam.

polation of these attributes to the year 2100. Our initial objective is to address these limitations. Upon resolving these problems, we can determine whether the ERSC experiences a higher or lower degree of warming than its neighbouring regions. Therefore, the present research findings are anticipated to generate significant interest and provide valuable insights for policymakers and decision-makers in formulating effective strategies and policies to address the challenges of shifting climatic conditions.

The present study implemented statistical downscaling approaches to anticipate the future climate over the northern region of the Egyptian Red Sea Coast (ERSC). Five locations within the study area, including Suez, Sharm El Sheikh, Hurghada, Safaga, and Marsa Alam, were selected to represent diverse climate conditions and a range of human activities. These locations were arranged from north to south, as shown in Figure 1.

2. Material and methods

Figure 2 illustrates the theoretical framework of the study, in which the first step involves utilising the observed data to depict the existing short-term fluctuations in surface air temperature (T_{2m}), relative humidity (RH), surface wind variables (WS_{10} and WD_{10}), and sea level pressure (SLP) from 2011 to 2021. Secondly, CDF matching for overlap years (2015–2021) between the observation and one ensemble member from each climate model [GFDL-ESM4 (USA); IPSL-CM6A-LR (France); MIROC6 (Japan); MRI-ESM2-0 (Japan)] was applied to remove bias from each model individually. Thirdly, the calculated bias correction statistical models were employed to downscale the future projections of the studied atmospheric parameters under the Shared Socioeconomic Pathways (SSPs) scenarios. After bias correction, the outputs of the individual climate models were averaged to calculate the ensemble mean for the period 2015–2100, thereby enhancing the accuracy and reliability of future projections at the five studied stations.

This approach utilised the Coupled Model Intercomparison Project Phase Six (CMIP6) to project weather parameter extremes on both global and regional scales. The latest version, CMIP6, has undergone significant advancements in parameterisation, physics, numerical methods, and configurations. It includes socioeconomic scenarios known as Shared Socioeconomic Pathways (SSPs), which enhance the reliability of climate projections. The improvements in CMIP6 encompass additional models and experiments, higher horizontal resolution, and lower biases compared to the earlier versions (Hamed et al., 2023).

2.1 Material

The process of developing accurate and reliable climate predictions is deeply dependent on data-driven insights. High-resolution observational datasets obtained from meteorological stations and satellite platforms play a fundamental role in both initialising climate models and verifying their performance. Such datasets not only improve the accuracy of representing current climate conditions but also strengthen predictive power by identifying key trends, patterns, and anomalies. These insights are essential for refining model parameters, minimising uncertainties, and generating reliable simulations of future climate scenarios (Tonbol, 2024).

2.1.1 Observed data

Five Automated Weather Observing Systems (AWOS) along the ERSC were used to collect T_{2m}, RH, WS_{10}, WD_{10}, and SLP at Suez, Sharm El Sheikh, Hurghada, Safaga, and Marsa Alam, as shown in Table 1. AWOS was installed and maintained according to World Meteorological Organisation (WMO) regulations. All readings were calculated to the WMO standard height, where the standard height is 0 m for SLP, 2m for T_{2m} and RH, and 10m for WS_{10} and WD_{10}. These five stations are well distributed spatially along the ERSC and provide hourly data from 2011 to 2021, with an average data gap across all studied parameters ranging from 5.5% to 7%, which is considered an acceptable percentage.

2.1.2 Modelled data (2010–2100)

The result of GFDL-ESM4 (USA; 1° × 1.2°), IPSL-CM6A-LR (France; 1.3° × 2.5°), MIROC6 (Japan; 1.4° × 1.5°), and MRI-ESM2-0 (Japan; 1.1° × 1.1°) climate models daily simulation of surface air temperature Tas, WS_{10}, and SLP are available on the Copernicus Climate Data Store (https://cds.climate.copernicus.eu/datasets/projections-cmip6?tab=download) through CMIP6 under different emission scenarios (SSP119, SSP 126, SSP 434, SSP 245, SSP 460, SSP 370, SSP 585). More details are available on (Boucher et al., 2018; Krasting et al., 2018; Tatebe and Watanabe, 2018; Yukimoto et al., 2019).

2.2 Methods

2.2.1 Observed data statistical analysis

The observed data for T_{2m}, RH, WS_{10}, WD_{10}, and SLP during 2011–2021 were subjected to statistical analysis (mean, standard deviation, minimum, and maximum) to investigate their temporal variation on hourly, daily, monthly, and annual bases. In addition, the wind rose software (Windographer 5.3) is used similarly to describe temporal variation in WD_{10}.

2.2.2 The CDF approach

The CDF approach is applied independently for each studied station. In accordance with Vigaud et al. (2013), the CDF approach can be used as follows: For weather station, let F_h represent the CDF of observed local data from 2015 to 2020 (calibration period) while the years 2021 is used for the validation processes between each used GCMs [GFDL-ESM4 (USA); IPSL-CM6A-LR (France); MIROC6 (Japan); MRI-ESM2-0 (Japan)] and observation; G_h represents the CDF of each used GCMs bi-linearly interpolated

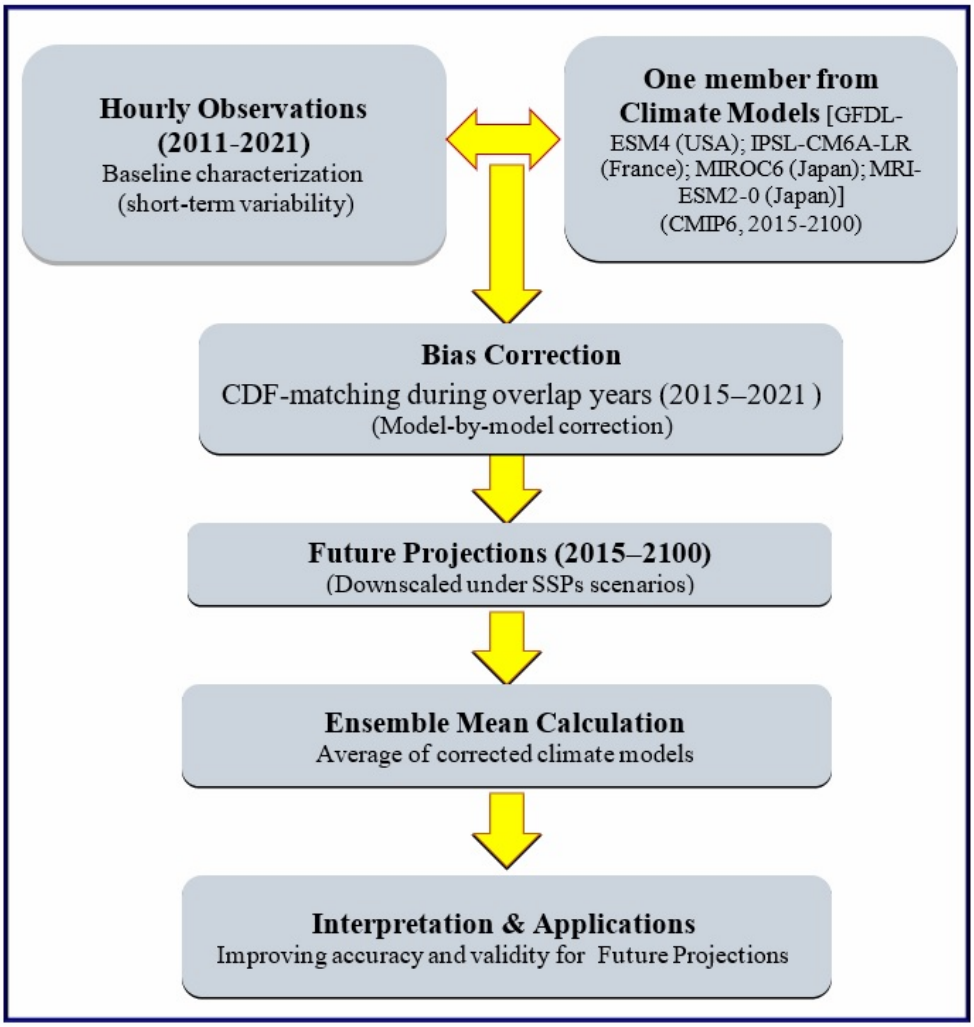

Figure 2. The theoretical framework (workflow).

at the same station location for the same period; and F_f and G_f represent their corresponding values for the future (2022–2100) for each studied global climate model outputs and observed outputs, respectively. Based on the presumption that a transformation T exists, transforming the CDF of one member from the used global climate model variables (predictor) into the CDF representing the observation (predictand) at the specified weather station, the bias correction technique is implemented T: $[0,1] \rightarrow [0,1]$

$$T(G_h(x)) = (F_h(x)) \quad (1)$$

Replacing x by ${G_h}^{-1}(u)$ in Equation (1) with $u \in [0,1]$ allows the following definition for the transform T:

$$T(u) = F_h({G_h}^{-1}(u)) \quad (2)$$

Assuming that this later relationship remains valid in the future (i.e. $F_f = T(G_f)$), the researched CDF is given by:

$$F_f(x) = F_h\left({G_h}^{-1}\left(G_f(x)\right)\right) \quad (3)$$

2.2.3 Statistical downscaling for future projection

Often, before conducting any research on the effects of climate change, climate simulations must be adjusted. Specifically, the output of Global Climate Models (GCMs) might be affected due to systemic biases inherent in the model. Regular temperature deviation is one of the common problems. These biases result from low geographical resolution, oversimplified thermodynamic processes, and insufficient understanding of the Earth's climate system. According to the Copernicus website (https://climate.copernicus.eu/sites/default/files/2021-01/infosheet7.pdf;accssed ,03-6-2024), using uncorrected model outputs in impact assessments can result in inflated forecasts. Therefore, considering the variations in the mean and variability between GCM and observations during a reference period, the Bias Correction technique is employed to correct the projected raw GCM output (Vaittinada Ayar, 2021).

The results of the four different climate models [GFDL-ESM4; IPSL-CM6A-LR; MIROC6; MRI-ESM2-0] were matched individually with daily observations during a con-

Table 1. Elevations and positions of Meteorological working stations. (Period of recorded data for all stations from 2011 to 2021). The identification numbers (IN) 1 to 5 are also included in Figure 1.

Station		Height above	Geographic position		International
Names	IN	sea level (m)	Latitude (N)	Longitude (E)	station number
Suez	1	13.48	29°52′14″	32°28′30″	62450
Sharm El Sheikh	2	50	27°58′38.24″	34°23′41.82″	62460
Hurgada	3	14	27°10′43″	33°48′2.99″	62463
Safaga	4	18	26°45′2″	33°57′10″	62466
MarsaAlam	5	77	25°33′25.56″	34°35′1.32″	62470

Table 2. Annual, monthly, and hourly characteristics for the parameters under study based on hourly observed data from 2011 to 2021 over Suez, Sharm El Sheikh, Hurghada, Safaga, and Marsa Alam.

Station		Surface air temperature (T_{2m}, °C)		Relative humidity (RH, %)		Surface wind speed (WS_{10}, m s^{-1})		Sea level pressure (SLP, hPa)	
		Max	Min	Max	Min	Max	Min	Max	Min
Suez	Annual	2014 25.05	2011 23.48	2014 52.40	2016 48.83	2011 2.25	2018 1.67	2019 1014.65	2014 1012.98
	Monthly	Aug. 31.00	Jan. 15.72	Dec. 54.55	May 43.30	Sep. 2.29	Jan. 1.51	Jan. 1019.44 1	July 007.48
	Hourly	at 1500 28.31	at 0500 20.34	at 0500 63.76	at 1500 34.74	at 1800 2.5	at 0400 1.3	at 1000 1015.12	at 1500 1012.29
Sharm El Sheikh	Annual	2021 27.38	2011 25.76	2019 51.43	2013 34.46	2017 5.01	2020 3.60	2019 1011.18	2018 1010.09
	Monthly	Aug. 33.77	Jan. 18.33	Nov. 46.74	May 32.62	June 5.60	Jan. 3.38	Jan. 1016.85	July 1003.68
	Hourly	at 1300 30.86	at 0300 23.11	at 0300 51.57	at 1300 30.68	at 0700 5.95	at 1700 3.11	at 0700 1012.10	at 1500 1009.48
Hurghada	Annual	2018 26.39	2011 24.95	2015 44.00	2021 35.17	2011 5.84	2019 4.21	2015 1012.11	2018 1010.95
	Monthly	Aug. 33.49	Jan. 16.81	Dec. 50.03	June 30.71	June 5.99	Nov. 4.19	Jan. 1017.90	Aug. 1004.29
	Hourly	at 1200 30.82	at 0400 21.28	at 0400 49.44	at 1200 31.72	at 0900 6.55	at 1900 3.95	at 0700 1012.86	at 1400 1009.90
Safaga	Annual	2018 26.57	2011 25.41	2020 44.81	2011 42.04	2011 6.16	2018 4.36	2015 1012.29	2012 1011.07
	Monthly	Aug. 0.60	Jan. 18.27	Oct. 47.27	June 39.92	Sep. 6.38	Jan. 4.48	Jan. 1018.11	July 1004.53
	Hourly	at 1300 28.28	at 0500 23.57	at 1700 48.78	at 0800 38.71	at 1100 7.47	at 2000 3.66	at 0800 1012.85	at 1500 1010.37
Marsa Alam	Annual	2012 26.38	2020 21.51	2020 48.42	2015 38.66	2021 6.48	2014 5.49	2020 1014.45	2018 1010.79
	Monthly	Aug. 2.86	Jan. 17.79	Nov. 54.34	June 27.80	June 6.69	Jan. 5.17	Jan. 1017.66	July 1004.95
	Hourly	at 1100 28.80	at 0300 22.54	at 1800 45.61	at 0900 35.38	at 1000 7.64	at 1800 4.09	at 0700 1012.73	at 1400 1010.50

trol period (2015–2021) using the CDF technique (Equation 2) to describe a simple statistical model for bias removal for each climate model separately. These individual statistical models were then applied to statistically downscale the studied atmospheric parameters up to 2100 under different future SSP scenarios. Subsequently, the results for each climate model after bias removal were averaged together to calculate the ensemble mean (S_D ensemble mean) from 2015 to 2100 with better accuracy and validity along ERSC (Equation 3) at the five studied stations. The future projections for the studied atmospheric parameters under the seven different SSPs future scenarios were calculated using the 30-year running average.

A t-test is used to evaluate whether the slope (b) of the regression line representing the GCMs trend is significantly different from zero at the 0.05 significance level. If the slope differs from zero, the trend is considered statistically significant: a positive slope ($b > 0, p < 0.05$) indicates an upward trend, a negative slope ($b < 0, p < 0.05$) indicates a downward trend, while a non-significant result ($p \geq 0.05$) suggests no evidence of a trend.

3. Results and discussion

3.1 Observed data

Table 2 shows annual, monthly, and hourly characteristics for T_{2m}, RH, WS_{10}, and SLP based on hourly observed data from 2011 to 2021 over Suez, Sharm El Sheikh, Hurghada, Safaga, and Marsa Alam.

3.1.1 Monthly time series

Monthly average time series for T_{2m}, RH, WS_{10}, and SLP based on hourly observed data from 2011 to 2021 over Suez, Sharm El Sheikh, Hurgada, Safaga, and Marsa Alam are shown in Figure 3.

T_{2m} data analysis showed that January 2012 was the coldest month during the study period at Suez, Sharm El Sheikh, Hurghada, and Safaga, with a value of 13.7°C, 16.7°C, 15.1°C, and 16.8°C, respectively. At Marsa Alam, the coldest month occurred in January 2020, with a value of 16.2°C. Conversely, August 2015 was the warmest month during the study period at Sharm El Sheikh, Hurghada, Safaga, and Marsa Alam, with a value of 35.1°C, 34.8°C, 33.6°C, and 34.2°C, respectively. At Suez, however, the warmest month was August 2019, with a value of 32.2°C.

RH data analysis revealed that the maximum monthly RH means during the study period occurred in January 2015 (61.7%), November 2019 (64%), November 2013 (58.7%), October 2015 (51.6%), and December 2017 (63.9%) at Suez, Sharm El Sheikh, Hurghada, Safaga, and Marsa Alam, respectively. Conversely, the lowest monthly mean RH during the study period were recorded in April 2016 (38.9%), June 2016 (25.2%), May 2019 (23.1%), April 2015 (35.8%), and May 2012 (24.3%) at Suez, Sharm El Sheikh, Hurghada, Safaga, and Marsa Alam, respectively.

WS_{10} data analysis showed that the windiest months during the study period were April 2011 (2.72 m s^{-1}), June 2017 (6.9 m s^{-1}), June 2015 (7.9 m s^{-1}), September 2016 (7.5 m s^{-1}), and September 2021 (8.06 m s^{-1}) at Suez, Sharm El Sheikh, Hurghada, Safaga, and Marsa Alam, respectively. Furthermore, January 2019 was the calmest month during the study period at Sharm El Sheikh and Safaga, with a value of 2.2 m s^{-1} and 2.1 m s^{-1}, respectively. At Suez, Hurgada, and Marsa Alam, the calmest months were December 2018 (0.9 m s^{-1}), December 2020 (3.0 m s^{-1}), and May 2020 (3.08 m s^{-1}), respectively.

SLP data analysis revealed that December 2015 recorded the maximum monthly SLP mean during the study period at Hurghada and Safaga, with values of 1020.0 hPa and 1020.2 hPa, respectively. In January 2020, Sharm El Sheikh and Marsa Alam reached 1018.9 hPa and 1019.4 hPa, respectively. At Suez, the maximum monthly SLP mean was 1022.5 hPa in December 2019. Conversely, July 2012 had the minimum monthly SLP mean during the study period at Sharm El Sheikh, Hurghada, Safaga, and Marsa Alam with a value of 1002.2 hPa, 1002.9 hPa, 1003.3 hPa, and 1003.9 hPa, respectively. At Suez, the minimum monthly SLP mean was 1005.8 hPa in July 2016.

Moreover, the wind rose provided a clear graphical representation of how WD_{10} varied monthly.

At Suez, the observed wind direction (WD_{10}) was predominantly north to southwest from December to March, while north to northwest winds dominated from April to November (Appendix 1, Figure 1).

At Sharm El Sheikh, the observed wind direction (WD_{10}) indicated that northerly winds were dominant throughout the year (Appendix 1, Figure 2).

At Hurgada, the observed wind direction (WD_{10}) was predominantly northwest from November to February, while north to northwest winds prevailed from March to October (Appendix 1, Figure 3).

At Safaga, the observed wind direction (WD_{10}) was mainly northwest from November to March, whereas north to northwest winds were dominant from April to October (Appendix 1, Figure 4).

At Marsa Alam, the observed wind direction (WD_{10}) was predominantly northwest from November to March, while northerly winds were dominant from April to October, as shown in Appendix 1 (Figure 5).

3.1.2 Annual time series

Annual average time series for T2m , RH, WS_{10}, and SLP based on hourly observed data from 2011 to 2021 over Suez, Sharm El Sheikh, Hurghada, Safaga, and Marsa Alam are shown in Figure 4.

T2m data analysis revealed that 2018 was the warmest year during the study period at Hurgada and Safaga, while at Suez, Sharm El Sheikh, and Marsa Alam, it was in 2014, 2021, and 2012, respectively. Likewise, 2011 was the coldest year at Sharm El Sheikh, Hurghada, and Safaga, while

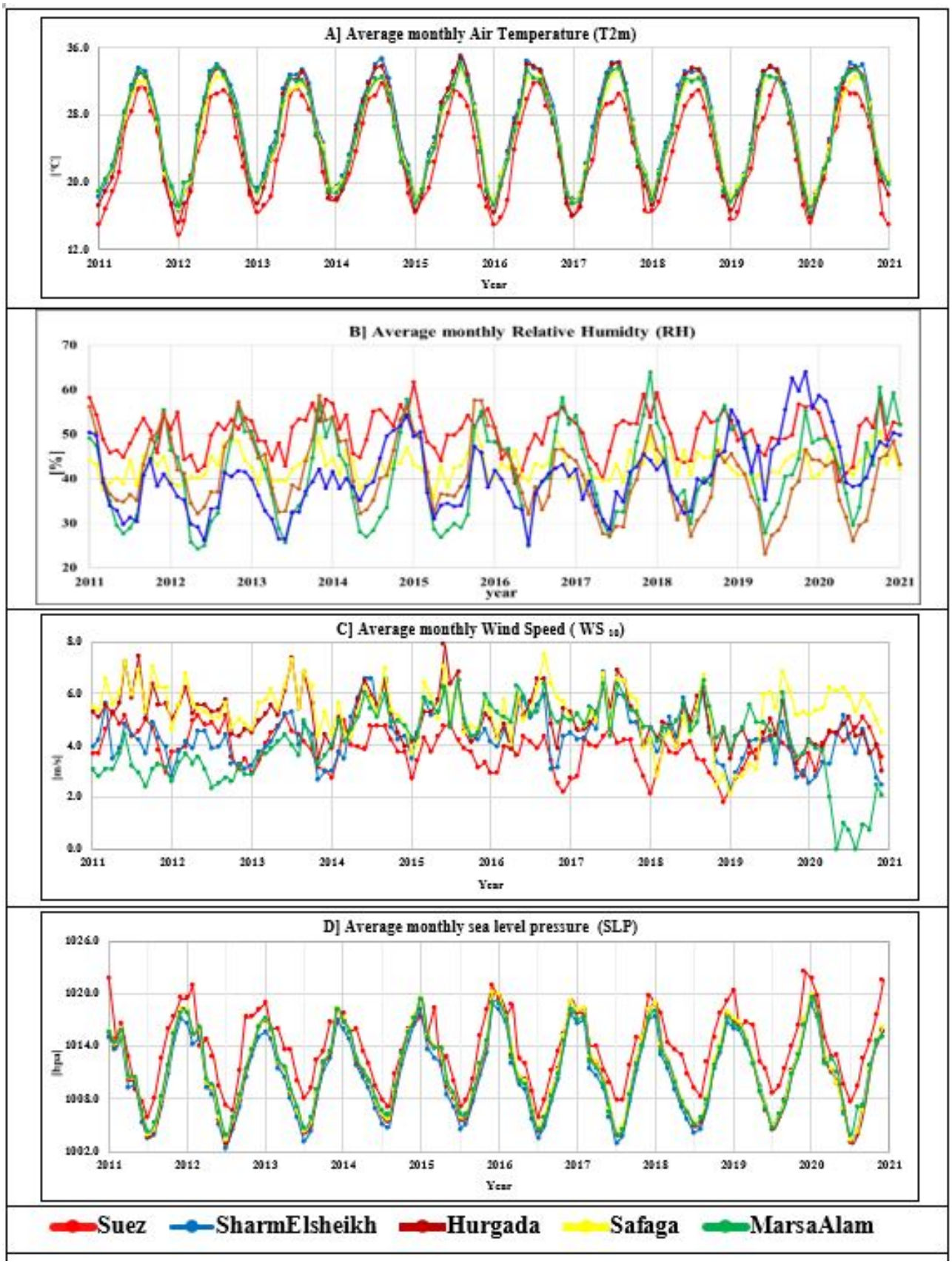

Figure 3. Monthly average time series for the parameters under study based on hourly observed data (2011–2021) over Suez, Sharm El Sheikh, Hurghada, Safaga, and Marsa Alam.

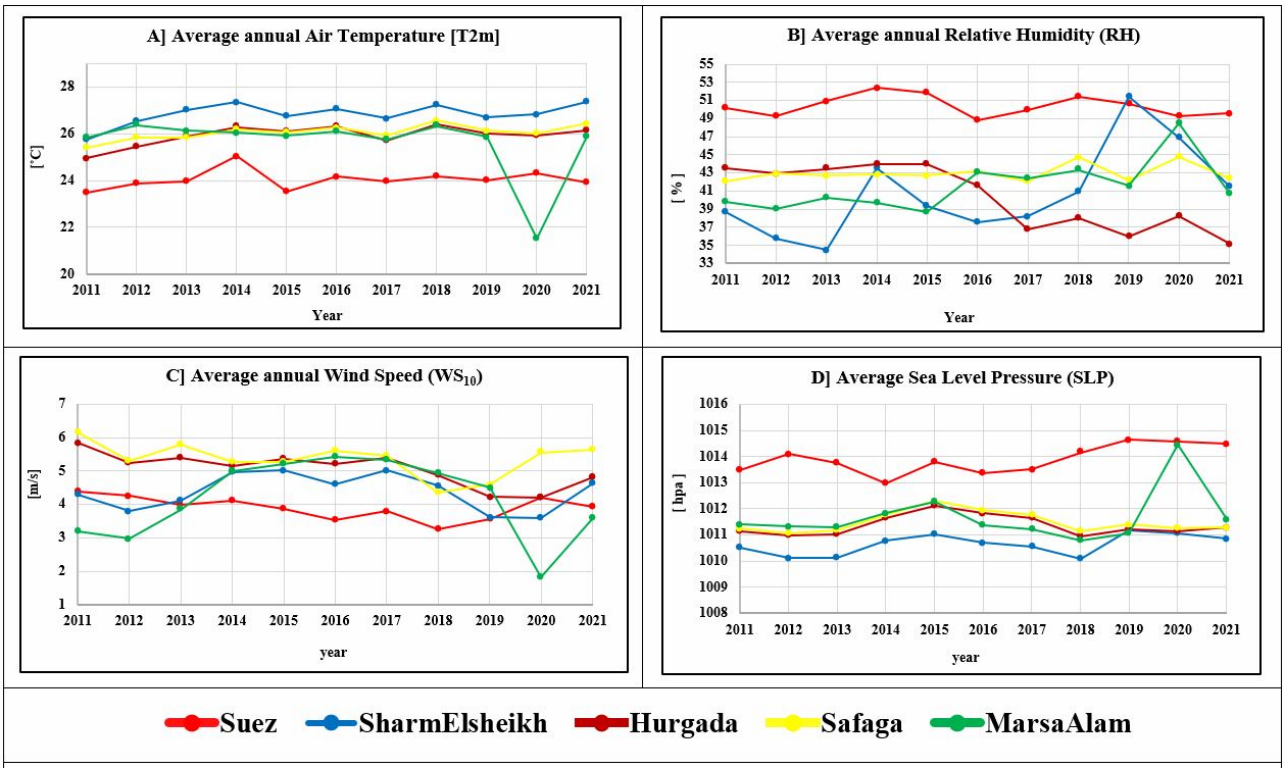

Figure 4. Annual average time series for the parameters under study based on hourly observed data (2011–2021) over Suez, Sharm El Sheikh, Hurghada, Safaga, and Marsa Alam.

Suez and Marsa Alam were in 2011 and 2020, respectively.

RH data analysis showed that 2020 had the highest annual average RH during the study period at Safaga and Marsa Alam, while at Suez, Sharm El Sheikh, and Hurghada, the highest values occurred in 2014, 2019, and 2015, respectively. On the other hand, the lowest annual average RH during the study period occurred during 2016, 2013, 2021, 2011, and 2015 at Suez, Sharm El Sheikh, Hurghada, Safaga, and Marsa Alam, respectively.

WS_{10} data analysis illustrated that 2011 recorded the maximum annual average of WS_{10} during the study period at Suez, Hurghada, and Safaga, while at Sharm El Sheikh and Marsa Alam, the maximum values were in 2017 and 2021, respectively. Conversely, 2018 recorded the minimum annual average WS_{10} at Suez and Safaga, while at Sharm El Sheikh, Hurghada, and Marsa Alam, the minimum values were observed in 2020, 2019, and 2014, respectively.

SLP data analysis confirmed that 2019 had the maximum annual average of SLP during the study period at Suez and Sharm El Sheikh, in 2015 at Hurghada and Safaga, and in 2020 at Marsa Alam. Furthermore, 2018 had the minimum annual average of SLP at Sharm El Sheikh, Hurghada, and Marsa Alam, while the minima at Suez and Safaga occurred in 2014 and 2012, respectively.

In general, the annual average T2m along the ERSC reached its maximum at Sharm El Sheikh (27.39°C), Safaga (26.57°C), Hurghada (26.39°C), Marsa Alam (26.38°C), and Suez (25.06°C). Conversely, the minimum annual average T2m was observed at Marsa Alam (21.51°C), Suez (23.48°C), Hurghada (24.95°C), Safaga (25.41°C), and Sharm El Sheikh (25.76°C).

The maximum annual average RH values were 52.4%, 51.43%, 48.42%, 44.81%, and 43.96% at Suez, Sharm El Sheikh, Marsa Alam, Safaga, and Hurghada, respectively. On the other side, the minimum values were 34.46%, 35.17%, 38.66%, 42.04%, and 48.83% at Sharm El Sheikh, Hurghada, Marsa Alam, Safaga, and Suez, respectively.

For WS_{10}, the horizontal distribution analysis showed that the maximum annual averages occurred at Marsa Alam, Safaga, Hurghada, Sharm El Sheikh, and Suez with a value of 6.48 m s^{-1}, 6.16 m s^{-1}, 5.84 m s^{-1}, 5.02 m s^{-1}, and 2.25 m s^{-1}, respectively. While the minimum annual averages were recorded at Suez (1.67 m s^{-1}), Sharm El Sheikh (3.60 m s^{-1}), Hurghada (4.23 m s^{-1}), Safaga (4.36 m s^{-1}), and Marsa Alam (5.49 m s^{-1}).

Regarding SLP, the maximum annual averages along the ERSC were 1014.65 hPa, 1014.45 hPa, 1012.29 hPa, 1012.11 hPa, and 1011.18 hPa at Suez, Marsa Alam, Safaga, Hurghada, and Sharm El Sheikh, respectively. In contrast, the minimum averages were 1010.08 hPa at Sharm El Sheikh, 1010.79 hPa at Marsa Alam, 1010.95 hPa at Hurghada, 1011.07 hPa at Safaga, and 1012.98 hPa at Suez.

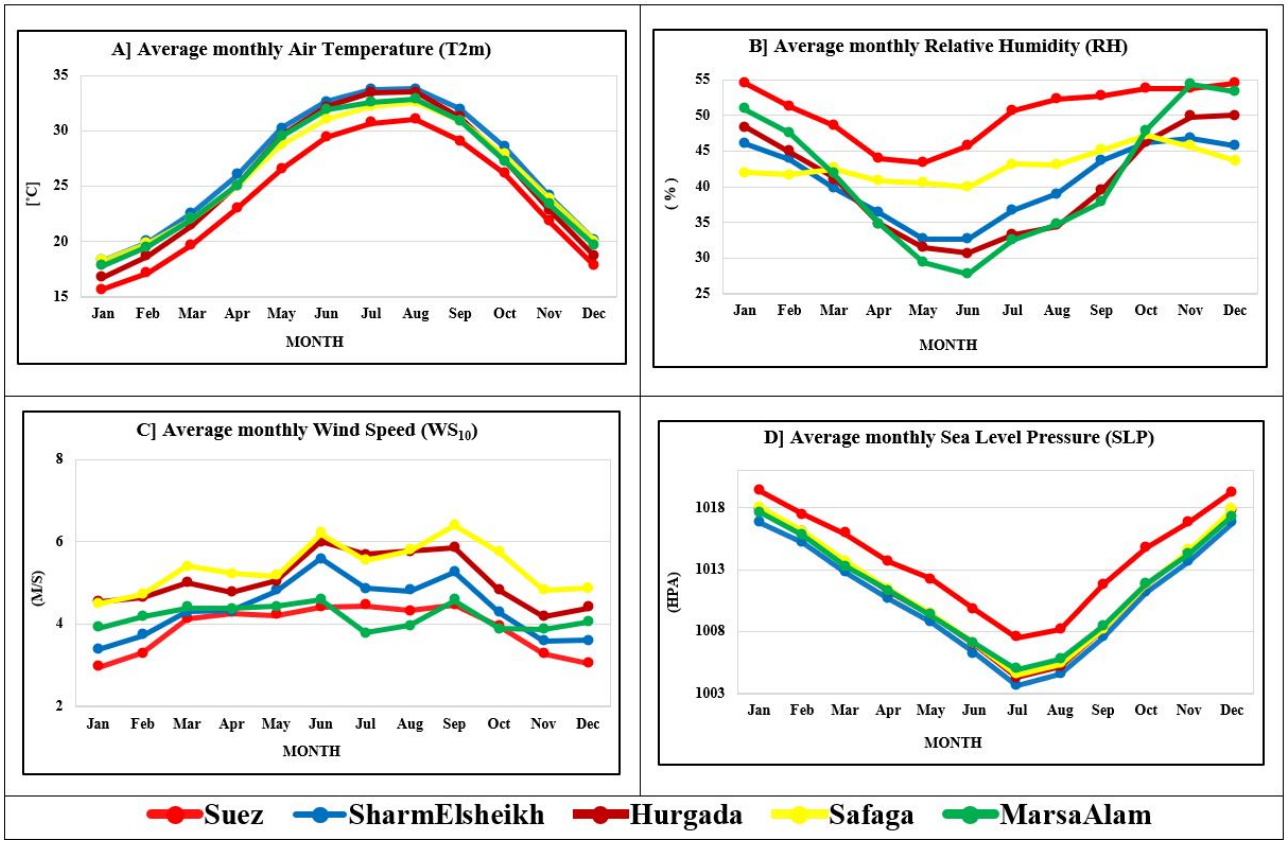

Figure 5. Observed short-term monthly means (Annual cycle) for the parameters under study based on hourly observed data (2011–2021).

Moreover, the wind rose diagram was employed as a graphical tool to illustrate the monthly variations in WD_{10}, as presented in Appendix 1 (Figure 6).

The wind direction (WD_{10}) over the study area was predominantly northwest from October to March, while north to northwest winds prevailed during the rest of the year. An exception was observed at Suez station, where north to southwest winds dominated from December to March.

3.1.3 Annual (Climate monthly average) and hourly cycle

The annual cycle (Climate monthly average) is described in Table 2 and illustrated in Figure 5. The annual T2m cycle reaches its maximum in August and its minimum in January across all five studied stations. The amplitude of the T2m annual cycle (MAX T2m – MIN T2m) ranges from 14.33°C at Safaga to 16.69°C at Hurghada.

The annual RH cycle reaches its maximum in October, November, and December at the five studied stations and its minimum value in May and June. The amplitude of the RH annual cycle varies from 7.31% at Safaga to 26.55% at Marsa Alam.

For WS_{10} analysis, the annual cycle shows maximum value in September at Safaga and Suez and in June at Hurghada, Sharm El Sheikh, and Marsa Alam. The minimum values occur in January at Suez, Sharm El Sheikh, Safaga, and Marsa Alam, and in November at Hurghada. The amplitude of the WS_{10} annual cycle ranges from 0.7 m s^{-1} at Suez to 2.22 m s^{-1} at Sharm El Sheikh.

Finally, the annual SLP cycle shows a maximum in January at all five stations, while the minimum occurs in July at all stations except Hurgada, where it occurs in August. The amplitude of the SLP annual cycle ranges from 11.96 hPa at Suez to 13.61 hPa at Hurghada.

Regarding the hourly cycle in Table 2 and Figure 6, the amplitude of the Daily T_{2m} cycle over Hurghada (9.54°C) was much higher than that over Suez (7.97°C), Sharm El Sheikh (7.75°C), Marsa Alam (6.26°C), and Safaga (4.71°C).

Similarly, the amplitude of the RH daily cycle over Suez (29.03%) was much higher than that over Sharm El Sheikh (20.88%), Hurghada (17.72%), Marsa Alam (10.23%), and Safaga (10.07%). Likewise, the amplitude of the WS_{10} daily cycle reached its maximum value (3.8 m s^{-1}) over Safaga, then Marsa Alam (3.25 m s^{-1}), Sharm El Sheikh (2.84 m s^{-1}), (2.61 m s^{-1}), while the minimum value was at Suez (2.27 m s^{-1}).

Finally, the amplitude of the SLP daily cycle reached its maximum value (2.96 hPa) over Hurgada, then Suez (2.83 hPa), Sharm El Sheikh (2.63 hPa), Safaga (2.48 hPa), and

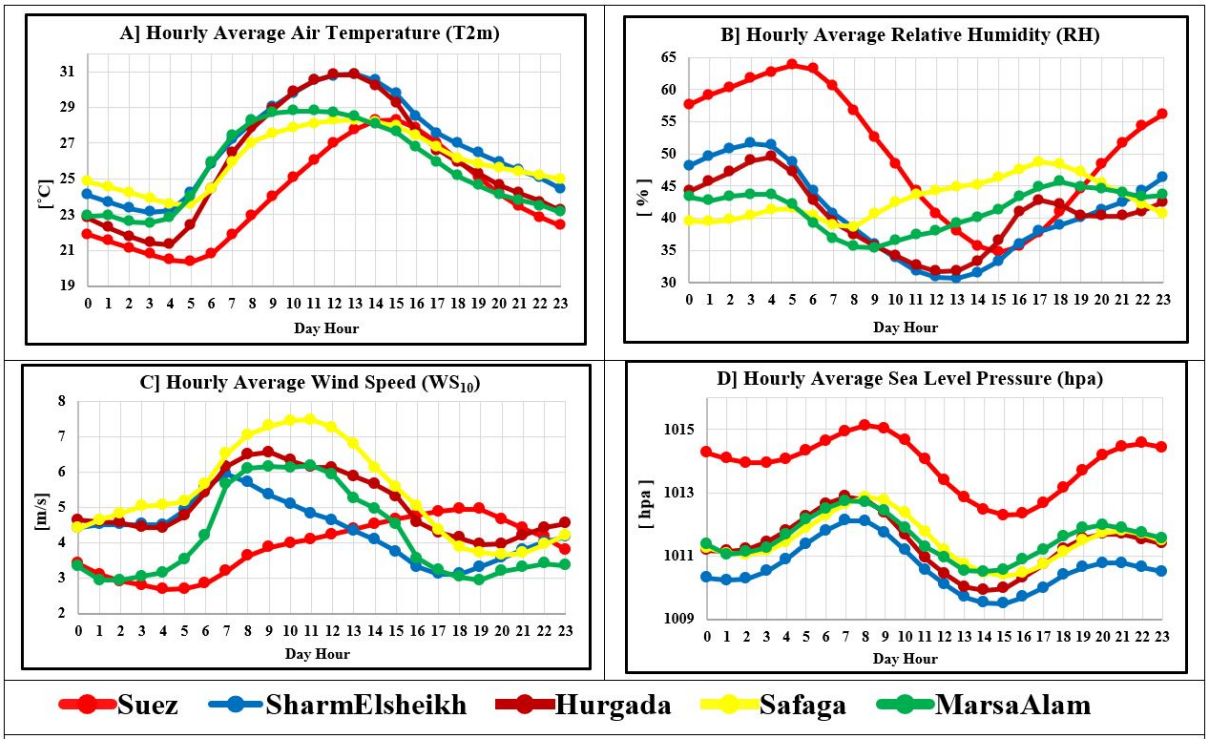

Figure 6. Observed short-term hourly means (Daily cycle) for the parameters under study based on hourly observed data (2011–2021).

the minimum value was at Marsa Alam (2.22 hPa).

In detail, the T_{2m} exhibited a diurnal cycle along ERSC, with the minimum occurring between 03:00–05:00, and the maximum occurring between 11:00–15:00. T_{2m} daily range was highest over Hurghada and lowest over Safaga (Figure 6A).

Generally, the RH exhibited a diurnal cycle over Suez and Sharm El Sheikh, with peak values occurring at 05:00 and 03:00, respectively, and lowest values recorded at 15:00 in Suez and 13:00 in Sharm El Sheikh. Similarly, RH exhibited a semi-diurnal cycle over Hurgada, Safaga, and Marsa Alam (Figure 6B).

The WS_{10} exhibited a diurnal cycle along ERSC, with the maximum values occurring between 07:00–10:00 at four stations, except at Suez, where it peaked at 18:00, and the minimum value occurring between 17:00–20:00 at four stations, except at Suez, where it reached its minimum at 04:00 (Figure 6C).

The SLP exhibited a semi-diurnal cycle along ERSC with two distinct maxima: the stronger occurring between 07:00 and 08:00, and a weaker one between 20:00 and 22:00. Conversely, SLP reached two distinct minima, with the lowest one occurring between 14:00 and 15:00, and a secondary minimum around 01:00 (Figure 6D).

The most notable result of this analysis is that the Suez station displayed a different pattern from the other stations, due to the Mediterranean Sea depression (also known as the Cyprus depression) and the influence of subtropical streams. In contrast, the other ERSC stations were primarily affected by tropical streams.

3.2 Statistical Downscaling for future projection

This section examines the results of ensemble mean simulations under various SSP scenarios for Tas (future surface air temperature scenarios), SFC (future wind speed scenarios), and PSL (future sea level pressure scenarios).

3.2.1 Bias correction for individual climate models under the control period, 2015–2021

A bias correction between one member of the used global climate model and the observations was calculated under the control period (2015–2021). Only SSP 119 was conducted for bias adjustment, as an example. However, due to the resemblance with SSP 119 during the control period, the bias correction for SSP 126, SSP 434, SSP 245, SSP 460, SSP 370, and SSP 585 are not shown.

As shown in Table 3, the GFDL-ESM4 model overestimated Tas across the five studied stations, ranging from 2.11°C (Marsa Alam) to 3.63°C (Suez). Conversely, the MIROC6 model underestimates Tas at the five studied stations, from 3.01°C(Suez) to 7.44°C (Marsa Alam). Similarly, the IPSL-CM6A-LR model closely simulates Tas over Hurgada, Safaga, and Marsa Alam, while overestimating Tas at Suez and Sharm El Sheikh by 2.92°C and 4.99°C, respectively. Moreover, the MRI-ESM2-0 model closely simulated Tas over Hurghada and Safaga, while overesti-

Table 3. Performance of different used modelsmodels used in the control period (2015–2021) variables over the studied stations: only the SSP 119 scenario is used. — means missing scenarios data.

Station	Model	Annual models mean – Annual observations		
		Surface air temperature (Tas,°C)	Surface wind speed (SFC, m s^{-1})	Sea level pressure (PSL, hPa)
Suez	GFDL-ESM4	3.63	−3.27	−0.72
	IPSL-CM6A-LR	2.92	−4.66	−1.03
	MIROC6	−3.01	—	5.13
	MRI-ESM2-0	1.37	—	−1.92
Sharm El Sheikh	GFDL-ESM4	3.97	−3.88	−2.38
	IPSL-CM6A-LR	4.99	−4.95	−3.83
	MIROC6	−5.28	—	4.63
	MRI-ESM2-0	2.65	—	−4.40
Hurghada	GFDL-ESM4	2.25	−0.64	−1.25
	IPSL-CM6A-LR	−0.02	−2.45	−0.84
	MIROC6	−6.18	—	5.37
	MRI-ESM2-0	0.48	—	−3.16
Safaga	GFDL-ESM4	2.44	−2.56	0.43
	IPSL-CM6A-LR	0.17	−4.36	0.83
	MIROC6	−5.99	—	7.04
	MRI-ESM2-0	0.67	—	−1.48
Marsa Alam	GFDL-ESM4	2.11	−1.35	−1.28
	IPSL-CM6A-LR	−0.16	−3.16	−0.87
	MIROC6	−7.44	—	6.18
	MRI-ESM2-0	−1.20	—	−2.44

mating Tas over Suez and Sharm El Sheikh by 1.37°C and 2.65°C, respectively, and underestimating Tas over Marsa Alam.

GFDL-ESM4 and IPSL-CM6A-LR models underestimated SFC across the five studied stations, with values ranging from 0.64 to 4.95 m s^{-1}. Data for MIROC6 and MRI-ESM2-0 were unavailable for certain scenarios. The GFDL-ESM4 and IPSL-CM6A-LR models closely simulated PSL along the study area, while the MIROC6 model overestimated PSL and the MRI-ESM2-0 model underestimated PSL.

The ensemble means, which are used to improve the reliability and reduce uncertainty, were calculated by averaging the results of the four GCMs used after bias removal, as the performance of these models differed for Tas, SFC, and PSL, and varied between stations (Table 3 and Appendix 2, Figures 1–4).

3.2.2 Future atmospheric parameters, 2030–2100

Based on the developed statistical model, which was obtained by matching the CDF of each used GCMs with the CDF of the observation during the validation period (2015–2020) for only SSP 119 scenario (the year 2021 used for verification), each GCMs at each site for the period 2015–2100 was subjected to bias removal to calculate S_D GCMs simulations (statistically downscaled GCM results). During 2021, the comparison of the corrected GCMs outputs with observations (data not shown) revealed that the bias correction using the CDF approach significantly improved consistency with the observed data. The corrected GCMs outputs captured monthly and seasonal variability with high correlation coefficients, and the mean bias decreased up to zero. The results indicate that the used statistical model not only fits closely with the calibration period, but it remains accurate when used on a different year. This supports the reliability of the CDF-based approach for future projections.

The statistically downscaled ensemble means (S_D_ensemble means) at each site for the period 2015–2100 were calculated by averaging the results of S_D_GCMs simulations. For each site along the ERSC, the calculated S_D_ensemble means were used to compute the atmospheric future projections more accurately. A 30-year running average was applied to generate future projections for the investigated parameters under the SSP future scenarios.

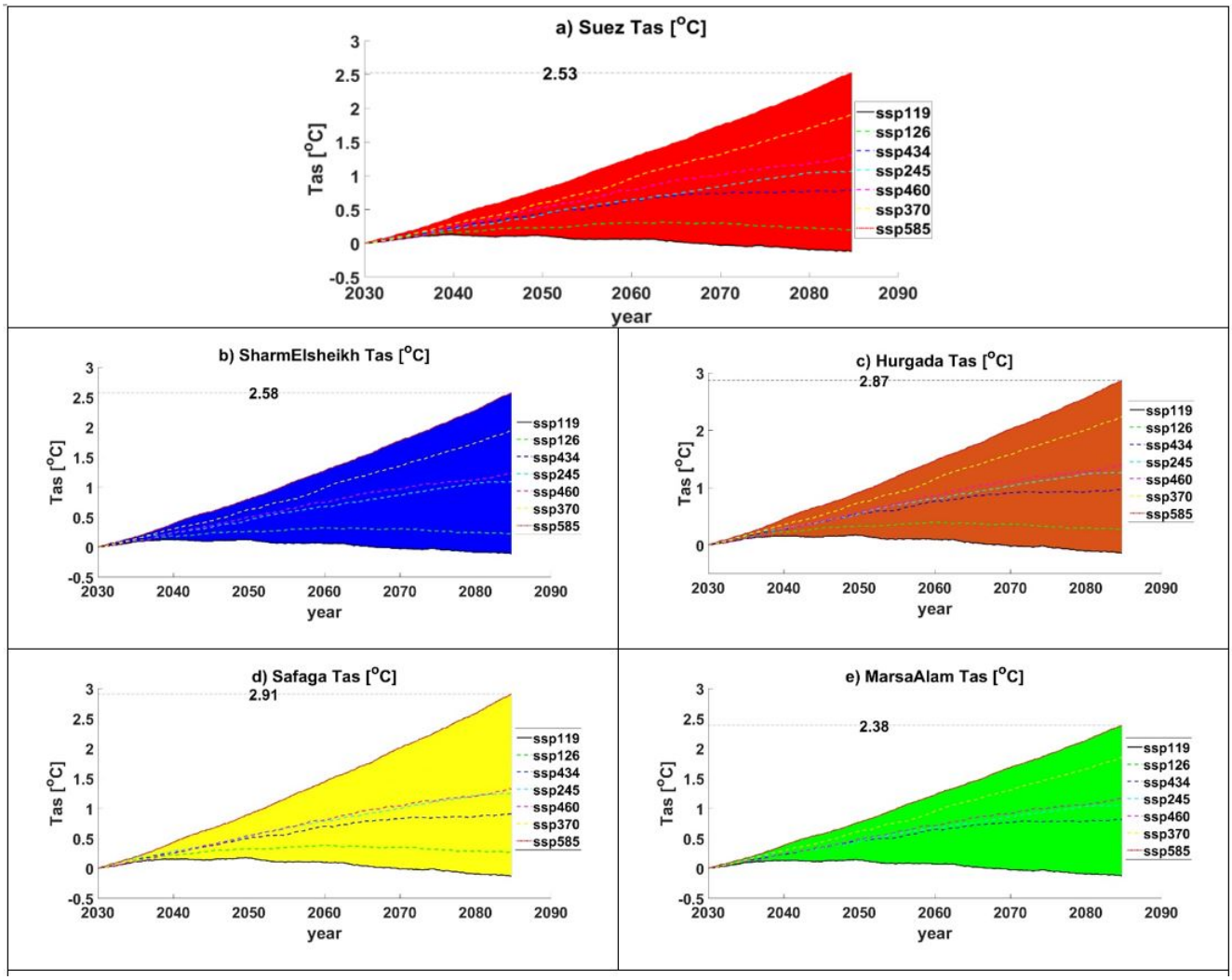

Figure 7. Thirty-year running annual means for surface air temperature (Tas) anomalies concerning the 2015–2021 averages for the statistically downscaled ensemble mean simulations.

Table 4. Tas trend for current century (°C/century): calculated as the difference between the projected surface air temperature (Tas) at the end of the current century and the average Tas value during 2015–2021.

Station	ssp119	ssp126	ssp434	ssp245	ssp460	ssp370	ssp585
Suez	−0.12	0.20	0.78	1.07	1.30	1.91	2.53
Sharm El Sheikh	−0.11	0.22	0.79	1.09	1.23	1.95	2.58
Hurghada	−0.14	0.27	0.96	1.27	1.39	2.24	2.87
Safaga	−0.13	0.27	0.91	1.25	1.32	2.18	2.91
Marsa Alam	−0.12	0.23	0.81	1.05	1.17	1.85	2.38

Table 5. STC trend for current century (m s^{-1}/century): calculated as the difference between the projected wind speed (STC) at the end of the current century and the average STC value during 2015–2021.

Station	ssp119	ssp126	ssp434	ssp245	ssp370	ssp585
Suez	0.061	0.012	0.030	0.038	−0.021	0.025
Sharm El Sheikh	.042	0.035	0.030	0.047	0.001	0.024
Hurghada	0.036	0.036	−0.011	0.039	0.025	0.006
Safaga	0.039	0.033	−0.012	0.035	0.020	0.002
Marsa Alam	0.069	0.018	−0.004	0.027	0.012	−0.002

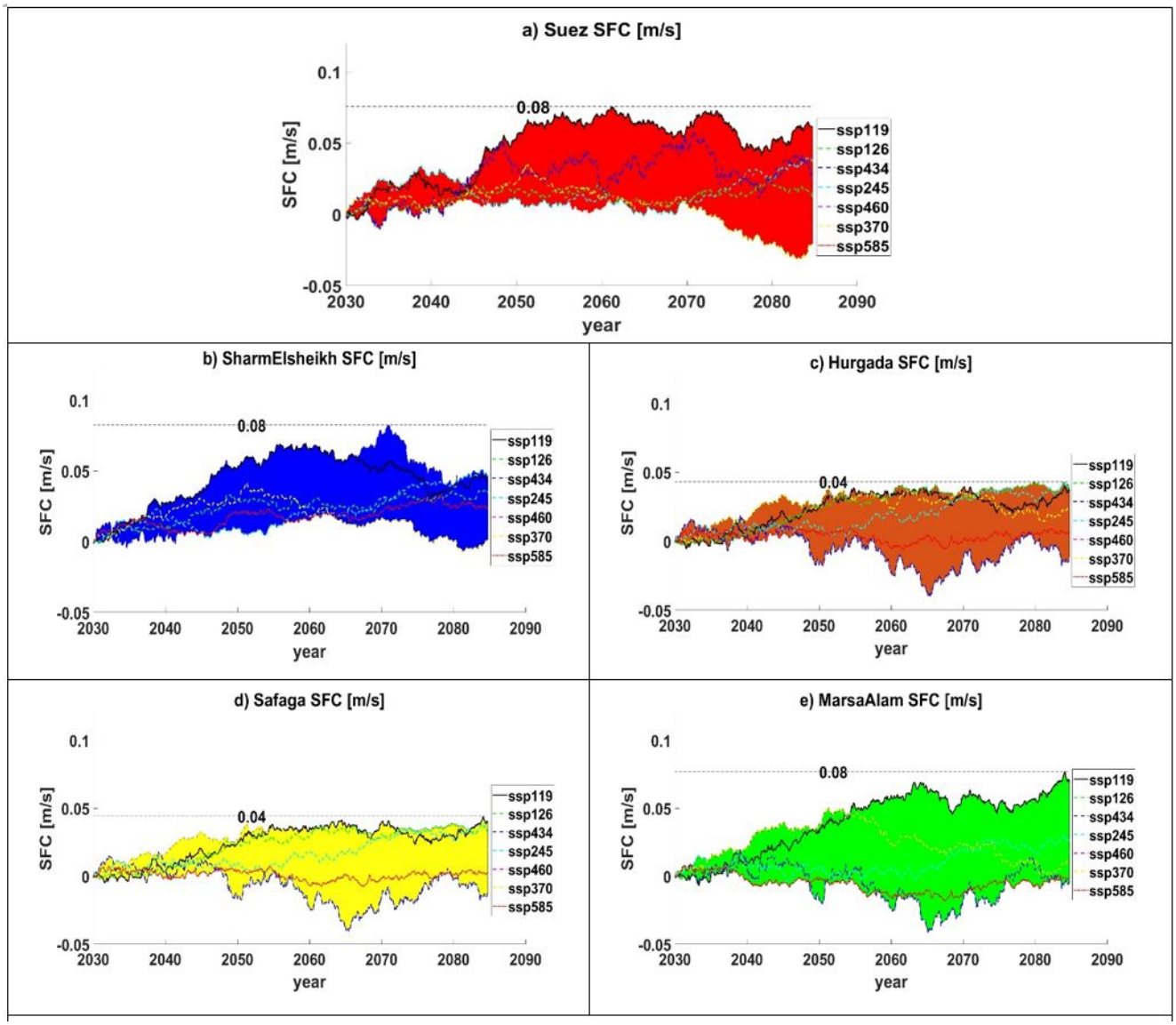

Figure 8. Thirty-year running annual means for surface wind speed (SFC) anomalies concerning the 2015–2021 averages for the statistically downscaled ensemble mean simulations.

S_D_ensemble means of projected Tas scenarios up to 2100 indicate significant warming along the ERSC, particularly for the SSP 585 scenario at Safaga, as shown in Figure 7. The projected warming at the end of the current century (concerning the 2011–2021 average values) exhibits the following trends: a negative trend ranging between −0.11°C at Sharm El Sheikh and −0.14°C at Hurgada under the SSP 119 scenario; a positive trend ranging between 0.20°C at Suez and 0.27°C at Sharm El Sheikh and Hurgada under the SSP 126 scenario, 0.78°C at Suez and 0.96°C at Hurgada under the SSP 434 scenario, 1.05°C at Marsa Alam and 1.27°C at Hurgada under the SSP 245 scenario, 1.17°C at Marsa Alam and 1.39°C at Hurgada under the SSP 460 scenario, 1.85°C at Marsa Alam and 2.24°C at Hurgada under the SSP 370 scenario, and 2.38°C at MarsaAlam and 2.91°C at Safaga under the SSP 585 scenario, as reported in Table 4.

According to IPCC (2023, p.12), the best estimates for the different scenarios are 1.4°C (SSP 119), 1.8°C (SSP 126), 2.7°C (SSP 245), 3.6°C (SSP 370), and 4.4°C (SSP 585) (Lee et al., 2023). Comparable to these IPCC estimates, the results of the current study indicate that the warming trend under various SSP scenarios is significantly lower than the global average by 1.52, 1.56, 1.55, 1.58, and 1.75°C per century for SSP 119, SSP 126, SSP 245, SSP 370, and SSP 585, respectively. This difference can be attributed to the Red Sea's unique oceanographic properties (narrow, semi-enclosed, and high evaporation rate), regional circulation patterns, and/or the subtropical high-pressure belt that characterises the study area.

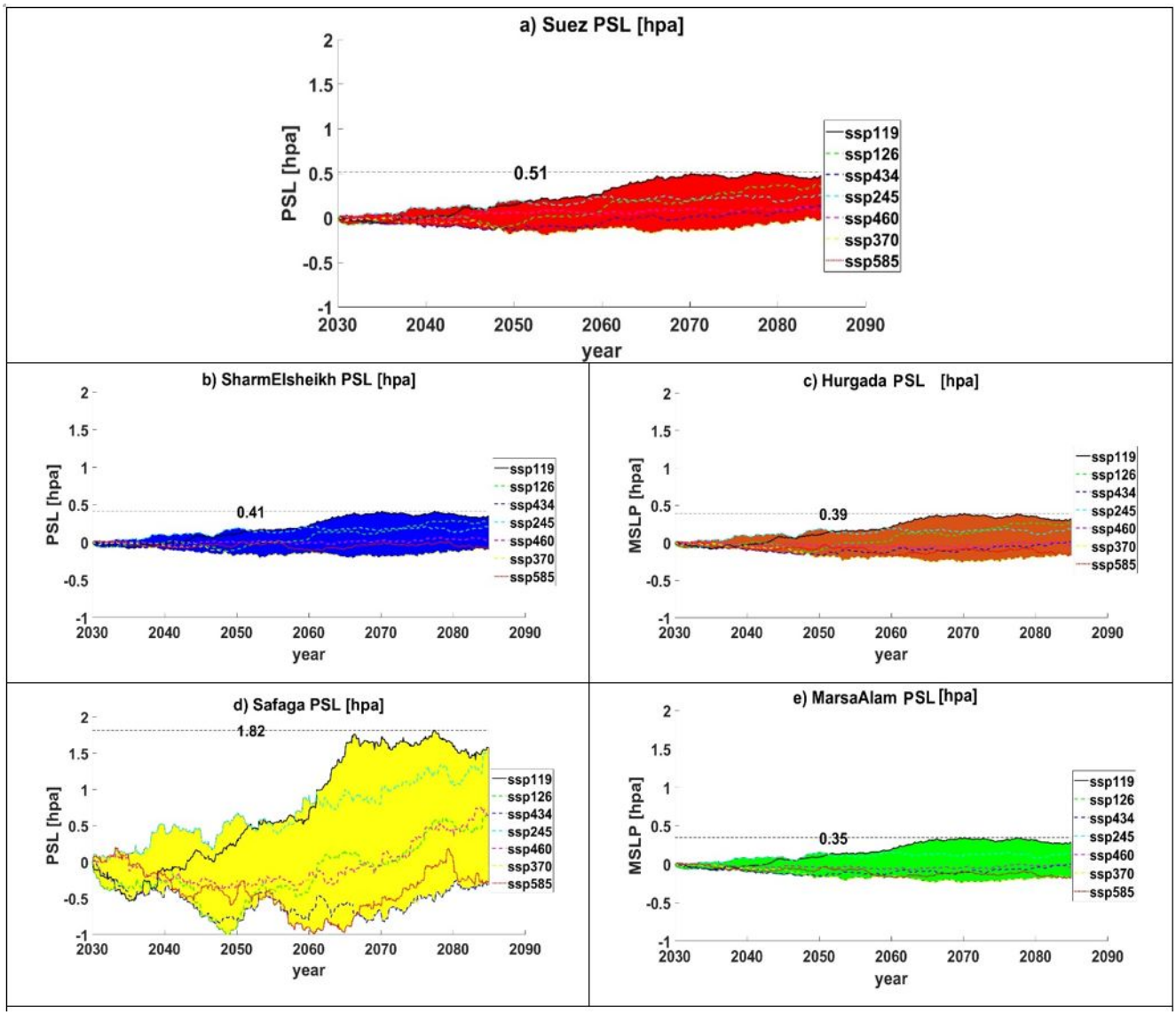

Figure 9. Thirty-year running annual means for sea level pressure (PSL) anomalies concerning the 2015–2021 averages for the statistically downscaled ensemble mean simulations.

The S_D_ensemble means of projected SFC scenarios up to 2100 along the ERSC shows variation in trend, as summarised in Table 5. Wind speed at the end of the current century (relative to the 2011–2021 average values) exhibits the following trends: a positive trend ranging between 0.036 m s^{-1} at Hurgada and 0.069 m s^{-1} at Marsa Alam under SSP 119; 0.012 m s^{-1} at Suez and 0.036 m s^{-1} at Hurgada under the SSP 126; −0.012 m s^{-1} at Safaga and 0.030 m s^{-1} at Suez and Sharm El Sheikh under the SSP 434; 0.027 m s^{-1} at Marsa Alam and 0.039 m s^{-1} at Hurgada under the SSP 245; −0.021 m s^{-1} at Suez and 0.025 m s^{-1} at Hurgada under the SSP 370; and −0.002 m s^{-1} at Marsa Alam and 0.025 m s^{-1} at Suez under the SSP 585 (Figure 8). These results indicate that the projected SFC will undergo a nonsignificant change up to 2100.

S_D_ensemble means of projected PSL scenarios up to 2100 along the ERSC show variations in trend, as summarised in Table **??**. At the end of the current century (relative to the 2011–2021 average values), PSL exhibits a positive trend under SSP119, ranging from 0.14 hPa at Marsa Alam to 0.67 hPa at Safaga, and under the SSP 126, ranging from 0.08 hPa at Marsa Alam to 0.33 hPa at Safaga. In contrast, negative trends are observed under SSP 434 (0.01 hPa at Suez to 0.55 hPa at Safaga), SSP 245 (0.07 hPa at Suez to 0.49 hPa at Safaga), SSP 460 (0.22 hPa at Suez to 1.31 hPa at Marsa Alam), SSP 370 (0.29 hPa at Suez to 1.52 hPa at Safaga), and SSP 585 (0.35 hPa at Suez to 1.95 hPa at Safaga) (Figure 9). These results indicate that the projected PSL will experience a nonsignificant trend under SSP 119 and SSP 126, whereas negative trends occur

under SSP 434, 245, 460, 370, and 585. The nonsignificant trends suggest that the atmospheric mass remains effectively unchanged up to 2100 under SSP 119 and SSP 126, while the negative trends suggest a potential decrease in atmospheric mass due to extensive warming processes under SSP 434, 245, 460, 370, and 585.

The novel findings of the current study are:

1. This research represents the first attempt to use statistical downscaling to project future climate conditions along the Egyptian Red Sea Coast, distinguishing it from previous studies that relied on dynamical downscaling. This approach enhances uncertainty analyses of future projections and provides a broader perspective on potential climate changes.

2. The study has international relevance, as Statistical downscaling has been applied in other arid and semi-arid coastal regions worldwide (e.g., along the Saudi Arabian Red Sea Coast (Bawadekji et al., 2022), Australian coast (Timbal and Fernandez, 2009), and the Egyptian Mediterranean coast (Elbessa and Shaltout, 2024)). Thus, the methodology used here can be applied to similar regions facing climate change risks, such as water scarcity and warming issues.

3. The current research has practical implications by providing policymakers and stakeholders with detailed information on future climate projections, which can support improved regional planning.

4. Conclusions

Unfortunately, only a few scientific studies have been published regarding climate change along the ERSC. These limited studies primarily focused on dynamical downscaling, highlighting the need for further research, particularly in statistical downscaling, to improve our understanding of both present and future climate conditions. Consequently, developing a precise statistical downscaling framework to simulate the climate along the ERSC would be highly beneficial for providing more reliable information to decision-makers. The present study offers a comprehensive analysis to address this gap in climate forecasting. Moreover, it presents a detailed examination of the atmospheric conditions in the study area based on recent in situ observations.

Observation data (2011–2021) were used together with model-by-model results from used four different global climate models [GFDL-ESM4 (USA); IPSL-CM6A-LR (France); MIROC6 (Japan); MRI-ESM2-0 (Japan)] for the period 2015–2100 to characterise recent surface atmospheric fluctuations along the ERSC and to develop a statistical downscaling model for projecting future climate changes. Finally, the ensemble means, obtained by averaging the bias-corrected outputs of the four applied GCMs, were employed to enhance result reliability and minimise uncertainty.

Data analysis revealed that air temperature exhibited a diurnal cycle, while RH showed a diurnal cycle over Suez and Sharm El Sheikh, and a semi-diurnal pattern was observed over Hurghada, Safaga and Marsa Alam. While SLP displayed a semi-diurnal cycle across all five studied stations. Moreover, the maximum air temperature occurred during August, while the surface relative humidity reached its peak in November and December, the surface wind speed reached its peak in September and June, and the highest sea level pressure was observed in January.

In general, the prevailing wind direction along the ERSC fluctuates between north to northwest, with significant monthly variation between the Northern and Northwesterly that is related to the mountainous nature of the Red Sea on both sides (East-West), supporting the previous results of (Elbessa et al., 2021). The new inference in this study about the wind speed was increased from 06:00 to 16:00 daily, related to the phenomena of sea breeze and anabatic winds.

Overall, the applied models tend to overestimate Tas while underestimating PSL and SFC during the control period (2015–2021). This behaviour highlights the importance of applying bias correction techniques, such as the CDF method, on a model-by-model basis to ensure validity for the study area.

Furthermore, the CDF technique was applied to statistically downscale each GCM individually [GFDL-ESM4, IPSL-CM6A-LR, MIROC6, and MRI-ESM2-0] along the ERSC. Subsequently, the ensemble mean was calculated from the bias-corrected simulations to enhance the reliability of the results. The projections indicate that the study area will experience significant warming and increased risks associated with heat stress. In the same context, PSL future scenarios exhibit negative trends, while the projected SFC is expected to undergo nonsignificant changes up to 2100.

The SSP future scenarios indicate that Tas trend during the current century ranges as follows: SSP 119 (−0.11 to −0.14°C), SSP 126 (0.20 to 0.27°C), SSP 434 (0.78 to 0.96°C), SSP 245 (1.05 to 1.27°C), SSP 460 (1.17 to 1.39°C), SSP 370 (1.85 to 2.24°C), and SSP 585 (2.38 to 2.91°C). In the same context, the SFC trend ranges as follows: SSP 119 (0.036 to 0.069 m s^{-1}), SSP 126 (0.012 to 0.036 m s^{-1}), SSP 434 (−0.012 to 0.030 m s^{-1}), SSP 245 (0.027 to 0.047 m s^{-1}), SSP 370 (−0.021 to 0.025 m s^{-1}), and SSP 585 (−0.002 to 0.025 m s^{-1}). Similarly, the PSL trend during the current century ranges as follows: SSP 119 (0.14 to 0.67 hPa), SSP 126 (0.08 to 0.33 hPa), SSP 434 (−0.55 to −0.01 hPa), SSP 245 (−0.49 to -0.07 hPa), SSP 460 (−1.01 to −0.22 hPa), SSP 370 (−1.52 to −0.29 hPa), and SSP 585 (−1.95 to −0.35 hPa).

Overall, the uncertainty in future warming is 3.05°C, with 91% attributed to scenario design and 9% to regional

variation. These results suggest that management actions should prioritise reducing greenhouse gas emissions. The uncertainty in future wind speed is 0.09 m s^{-1}; 37% is associated with regional variation, and 63% with scenario design. This behaviour demonstrates that any future sustainability planning should take regional variability into account. The uncertainty in future sea level pressure is 2.62 hPa, with 38% associated with scenario design and 62% with regional variation.

The Suez station showed a distinct tendency compared to the other ERSC stations under study, related to the Mediterranean Sea depression (also known as the Cyprus depression) and the influence of subtropical air streams, whereas tropical air streams affected the other ERSC stations.

No scenarios were created for relative humidity changes, as it is a dependent variable that relies on temperature and moisture content. In the current study, projected temperature, surface wind, and pressure changes have already been considered. At the same time, moisture content will be addressed in future work, as its analysis requires a more detailed investigation beyond the scope of this paper.

The present work is considered the first attempt to downscale the future climate along with ERSC statistically. The current results, with previously published dynamical downscaling results (Elbessa et al., 2021), especially in the Suez Gulf, enrich our understanding of the uncertainties associated with the future climate. Moreover, the authors intend to expand the statistical tool they studied to cover the ERSC. Finally, the current research highlights the importance of studying the effect of climate change on the coastal zone, industrial, and tourism sectors.

In future studies, the authors will expand the current work to include additional stations distributed throughout the ERSC to obtain a complete picture of the future uncertainties in the ERSC. Moreover, using a regional climate model as a scientific tool for dynamical downscaling will be considered in future work.

Additionally, a data centre should be established to compile data from all relevant authorities, facilitating research on climate change and its impact on Egypt.

In the future, the study should be expanded to include additional stations distributed throughout the ERSC to obtain a comprehensive assessment of future uncertainties in the region.

Acknowledgements

The authors would like to thank the ERASMUS+ AquaVET project (No. 101179739).

Conflict of interest

None declared.

Supplementary materials

Supplementary data associated with this article can be found online. Please follow this link to see the supplementary data associated with this article.

References

Abualnaja, Y., Papadopoulos, V.P., Josey, S.A., Hoteit, I., Kontoyiannis, H., Raitsos, D.E., 2015. *Impacts of climate modes on air–sea heat exchange in the Red Sea*. J. Climate 28 (7), 2665–2681. https://doi.org/10.1175/JCLI-D-14-00379.1

Acker, F., 2008. *New findings on unconscious versus conscious thought in decision making: additional empirical data and meta-analysis*. Judgment. Decis. Make. 3 (4), 292–303. https://doi.org/10.1017/S1930297500000863

Al-Barakati, A.M., James, A.E., Karakas, G., 2002. *A three-dimensional hydrodynamic model to predict the distribution of temperature, salinity, and water circulation of the Red Sea*. J. King Abdulaziz Univ. Mar. Sci. 13 (1). 3–16. https://doi.org/10.4197/MAR.13-1.1

Al-Subhi, A.M., Al-Aqsum, M.M., 2008. *Temporal and spatial variations of remotely sensed Sea surface temperature in the northern Red Sea*. J. King Abdulaziz Univ. Mar. Sci. 19 (1), 61–74. https://doi.org/10.4197/mar.19-1.5

Ayman, M., Salah, Z., Tonbol, K., Shaltout, M., 2023. *Evaluating ERA5 Weather Parameters Data Using Remote Sensing and in Situ Data Over the North Red Sea*. Int. Arch. Photogramm. Remote Sens. Spat. Inf. Sci. 48, 77–84. https://doi.org/10.5194/isprs-archives-XLVIII-1-W2-2023-77-2023

Bawadekji, A., Tonbol, K., Ghazouani, N., Becheikh, N., Shaltout, M., 2022. *Recent atmospheric changes and future projections along the Saudi Arabian Red Sea Coast*. Sci. Rep.12 (1), 160. https://doi.org/10.1038/s41598-021-04200-z

Boucher, O., Denvil, S., Levavasseur, G., Cozic, A., Caubel, A., Foujols, M.A., Meurdesoif, Y., Gastineau, G., 2018. *IPSL IPSL-CM6A-LR model output prepared for CMIP6 CMIP*. Earth System Grid Federation. https://doi.org/10.22033/esgf/cmip6.1534

Bruckner, A., Rowlands, G., Riegl, B., Purkis, S., Williams, A., Renaud, P., 2012. *Atlas of Saudi Arabian Red Sea Marine Habitats*. Panoramic Press Phoenix. AZ, USA.

Chaidez, V., Dreano, D., Agusti, S., Duarte, C.M., Hoteit, I., 2017. *Decadal trends in Red Sea maximum surface temperature*. Sci. Rep. 7:8144, 1–8. https://doi.org/10.1038/s41598-017-08146-z

Dawod, G., Amin, A., Haggag, G.G., 2022. *Variations of sea levels and atmospheric parameters along the Egyptian coasts over 2008–2020*. J. Sci. Eng. Res. 9 (5), 85–100.

Edwards, F.J., 1987. *Climate and Oceanography, Key Environments: Red Sea*. Pergamon Press, Oxford. 1, 45–68.

El Saman, M.I., Mahmoud, M.A., 2016. *Factors Affecting the Weather and Oceanography Parameters in Different Structural Areas of the Red Sea, Egypt*. Univ. J. Environ. Res. Technol. 6(2), 43–53.

Eladawy, A., Nadaoka, K., Negm, A., Abdel-Fattah, S., Hanafy, M., Shaltout, M., 2017. *Characterization of the northern Red Sea's oceanic features with remote sensing data and outputs from a global circulation model*. Oceanologia 59 (3), 213-237. https://doi.org/10.1016/j.oceano.2017.01.002

ElBessa, M., Abdelrahman, S.M., Tonbol, K., Shaltout, M., 2021. *Dynamical downscaling of surface air temperature and wind field variabilities over the Southeastern Levantine basin, Mediterranean Sea*. Climate 9 (10), 150. https://doi.org/10.3390/cli9100150

ElBessa, M., Shaltout, M., 2024. *Statistical downscaling of global climate projections along the Egyptian Mediterranean coast*. Oceanologia 66 (4), 66401, 25 pp. https://doi.org/10.5697/OBOE5006

Fowler, H.J., Blenkinsop, S., Tebaldi, C., 2007. *Linking climate change modeling to impacts studies: Recent advances in downscaling techniques for hydrological modeling*. Int. J. Climatol. 27(12), 1547–1578. https://doi.org/10.1002/joc.1556

Fouda, M.M., Gerges, M.A., 1994. *Implications of climate change in the Red Sea and Gulf of Aden region: an overview*.

Gad, M., Eid, F., El-Din, S.S., Radwan, A., Soliman, G., 2019. *Estimation of the Salt Storage and the Salt Content in the Gulf of Suez*. J. King Abdulaziz Univ. Mar. Sci. 29 (1), 37–51. https://doi.org/10.4197/Mar.29-1.3

Hamed, M.M., Salehie, O., Nashwan, M.S., Shahid, S., 2023. *Projection of temperature extremes of Egypt using CMIP6 GCMs under multiple shared socioeconomic pathways*. Environ. Sci. Pollut. Res.30, 38063–38075. https://doi.org/10.1007/s11356-022-24985-4

Hochman, A., Marra, F., Messori, G., Pinto, J. G., Raveh-Rubin, S., Yosef, Y., Zittis, G., 2022. *Extreme weather and societal impacts in the eastern Mediterranean*. Earth Syst. Dynam. 13 (2), 749–777. https://doi.org/10.5194/esd-13-749-2022

Jiang, H., Farrar, J.T., Beardsley, R.C., Chen, R., Chen, C., 2009. *Zonal surface wind jets across the Red Sea due to mountain gap forcing along both sides of the Red Sea*. Geophys. Res. Lett. 36, L19605. https://doi.org/10.1029/2009GL040008

Kaunang, T., Medellu, C.S., 2013. *Fluctuation of daytime air humidity in the mangrove forest edges*. J. Biol. Agric. Healthc. 3 (13), 154–159.

Krasting, J.P., John, J.G., Blanton, C., McHugh, C., Nikonov, S., Radhakrishnan, A., Rand, K., Zadeh, N.T., Balaji, V., Durachta, J., Dupuis, C., 2018. *NOAA-GFDL GFDL-ESM4 model output prepared for CMIP6 CMIP*. Earth System Grid Federation. https://doi.org/10.22033/ESGF/CMIP6.1407

Langodan, S., Cavaleri, L., Vishwanadhapalli, Y., Pomaro, A., Bertotti, L., Hoteit, I., 2017. *IPCC, 2023: The climatology of the Red Sea–part 1: the wind*. Int. J. Climatol. 37, 4509–4517. https://doi.org/10.1002/joc.5103

Lee, H., Calvin, K., Dasgupta, D., Krinner, G., Mukherji, A., Thorne, P.W., Trisos, C., Romero, J., Aldunce, P., Barrett, K., Blanco, G., Cheung, W.W., 2023. *Climate change 2023: synthesis report*. IPCC, 2023: Contribution of working groups I, II, and III to the sixth assessment report of the Intergovernmental Panel on Climate Change. The Australian Nat. Univ.

Maraun, D., Wetterhall, F., Ireson, A.M., Chandler, R.E., Kendon, E.J., Widmann, M., Brienen, S., Rust, H.W., Sauter, T., Themeßl, M., Venema, V.K.C., 2010. *Precipitation downscaling under climate change: Recent developments to bridge the gap between dynamical models and the end user*. Rev. Geophys. 48(3). RG3003. https://doi.org/10.1029/2009RG000314

Menezes, V.V., Farrar, J.T., Bower, A.S., 2018. *Westward mountain-gap wind jets of the northern Red Sea as seen by QuikSCAT*. Remote Sens. Environ. 209, 677–699. https://doi.org/10.1016/j.rse.2018.02.075

Michel, D., Pandya, A., 2010. *Coastal zones and climate change* Henry L. Stimson Center, Washington, 106 pp.

Middleton, N.J., Thomas, D.S., 1992. *World atlas of desertification*.

Mohammed, T., Dar, M.A., El-Saman, M.I., 2010. *Distribution patterns of hard and soft corals along the Egyptian Red Sea Coast*. Egypt. J. Aquat. Res. 36, 543–555.

Patzert, W.C., 1974. *Wind-induced reversal in Red Sea circulation*. Deep-Sea Res. Oceanogr. Abstr. 21 (2), 109–121. https://doi.org/10.1016/0011-7471(74)90068-0

Pedgley, D., 1974. *An outline of the weather and climate of the Red Sea*. Océanogr. Phys. Mer Rouge Paris, France, UNESCO, 9–27.

Sherwood, S.C., Huber, M., 2010. *An adaptability limit to climate change due to heat stress*. Proc. Natl. Acad. Sci. 107 (21), 9552–9555. https://doi.org/10.1073/pnas.0913352107

Sofianos, S.S., Johns, W.E., 2007. *Observations of the summer Red Sea circulation*. J. Geophys. Res. 112, C06025. https://doi.org/10.1029/2006JC003886

Tatebe, H., Watanabe, M., 2018. *MIROC MIROC6 model output prepared for CMIP6 CMIP*. Earth System Grid Federation. https://doi.org/10.22033/ESGF/CMIP6.881

Timbal, B., Fernandez, E., Li, Z., 2009. *Generalization of a statistical downscaling model to provide local climate change projections for Australia, Environmental Modelling and Software*. Environ. Model. Softw. 24 (3),

341–358.
https://doi.org/10.1016/j.envsoft.2008.07.007

Tonbol, K.M., El-Geziry, T.M., Elbessa, M., 2019. *Assessment of weather variability over Safaga harbor, Egypt. Arab*. J. Geosci. 12, 805.
https://doi.org/10.1007/s12517-019-4974-z

Tonbol, K., 2024. *Climate change: interdisciplinary solutions for a global challenge.* Multidisc. Adaptive Clim. Insights 1(1), 1–10.
https://doi.org/10.21622/MACI.2024.01.1.907

Turki, J.A., Al-Subh, A.M., Madah, F., 2023. *Influence of Tokar Gap wind jet on latent heat flux of Central Red Sea: empirical orthogonal function approach*. Ocean Coast. Res. 71(13), e23029.
https://doi.org/10.1590/2675-2824071.220103jat

United Nations Educational, Scientific, and Cultural Organization, 1979. *Map of the world distribution of arid regions*. MAB Tech. Notes 7, UNESCO, Paris, 54 pp.

Vaittinada, A.P., Vrac, M., Mailhot, A., 2021. *Ensemble bias correction of climate simulations: preserving internal variability*. Sci Rep. 11(1), 3098.
https://doi.org/10.1038/s41598-02182715-1

Vigaud, N., Varc, M., Caballero, Y., 2013. *Probabilistic downscaling of GCM senarios over southern India*. Int. J. Climatol. 33 (5), 1248–1263.
https://doi.org/10.1002/joc.3509

Viswanadhapalli, Y., Dasari, H.P., Langodan, S., Challa, V.S., Hoteit, I., 2017. *Climatic features of the Red Sea from a regional assimilative model*. Int. J. Climat. 37, 2563–2581.
https://doi.org/10.1002/joc.4865

Wilby, R.L., Wigley, T.M.L., 1997. *Downscaling general circulation model output: A review of methods and limitations*. Prog. Phys. Geogr. 21(4), 530–548.
https://doi.org/10.1177/030913339702100403

Yukimoto, S., Koshiro, T., Kawai, H., Oshima, N., Yoshida, K., Urakawa, S., Tsujino, H., Deushi, M., Tanaka, T., Hosaka, M., Yoshimura, H., 2019. *MRI-ESM2.0 model output prepared for CMIP6 CMIP. Earth System Grid Federation*.
https://doi.org/10.22033/ESGF/CMIP6.621